Stable Rb-B compounds under high pressure

Peiyu Zhang,[1] Yifan Tian,[1] Yilin Yang,[1] Hanyu Liu,[1,2] and Guangtao Liu [1,*]
[1]International Center for Computational Method & Software and State Key Laboratory of Superhard Materials, College of Physics, Jilin University, Changchun 130012, China
[2]Key Laboratory of Physics and Technology for Advanced Batteries (Ministry of Education), College of Physics, Jilin University, Changchun 130012, China

(Received 8 October 2022; revised 24 November 2022; accepted 6 January 2023; published 21 February 2023)

As a frontier issue of physics and material, the structures and related properties of borides have been extensively investigated in fundamental science. The search for pressure-induced stable compounds has become a feasible approach to acquire borides that are inaccessible at atmospheric pressure. Combined with state-of-the-art swarm intelligence structure prediction and first-principles calculations, we systematically explored the Rb-B system and uncovered a series of unprecedented RbB, Rb_2B_3, RbB_3, RbB_6, RbB_8, and RbB_{10} under high pressure. It is found that the catenation of boron evolves from linear chain to layered sheets, clusterlike units, and further to three-dimensional tunnel structures with increasing boron content. Among them, RbB_6 and RbB_8 are expected phonon-mediated superconductors with T_c of ∼12 K and superhard material with a hardness of ∼37 GPa at ambient pressure, respectively. Additionally, RbB_8 is a suitable precursor for obtaining the superconducting *o*-B_{16} boron allotrope by removing Rb due to its better stability than isomorphic SrB_8. The current results provide insights into the design of unforeseen borides and illustrate intriguing B-B bonding features originating from Rb → B charge transfer under pressures.

DOI: 10.1103/PhysRevResearch.5.013130

I. INTRODUCTION

Boron-based materials often show fascinating structural complexity due to the electron-deficient nature of boron [1,2]. Heretofore, hundreds of binary metal borides have been reported and attracted wide attention because of their outstanding properties for potential applications. Among these borides, MgB_2 was found to be an archetypal Bardeen-Cooper-Schrieffer (BCS) superconductor with the highest superconducting critical temperature (T_c) of 39 K at ambient pressure [3], which has triggered a flurry of explorations on the superconducting borides [4]. To date, many metal boride superconductors have been synthesized [5–10] or predicted [11–16], including YB_6 (7.2 K) [5], OsB_2 (2.1 K) [6], RuB_2 (1.6 K) [6], FeB_4 (2.9 K) [7], YB_{12} (4.5 K) [8], ZrB_{12} (6 K) [8,9], MoB_2 (32 K) [10], CaB_2 (∼50 K) [11], LaB_8 (14 or ∼20 K) [12,13], BeB_6 (24 K) [14], MgB_6 (9.5 K) [15], and LiBC (65 K) [16]. In addition, some transition-metal borides have been suggested as superhard materials owing to their high valence-electron density and strong covalent bonds [17–19], such as ReB_2 [20], OsB_2 [21], WB_4 [22], CrB_4 [23], FeB_4 [7], ZrB_{12} [24], $Zr_{0.5}Y_{0.5}B_{12}$ [8], YB_6 [25], ScB_3, and ScB_6 [26], most of whose hardness values have been measured to > 40 GPa. Furthermore, highly symmetrical cubic MB_6 compounds (M = alkaline-earth and rare-earth metals) also exhibit other compelling behaviors such as low work function (LaB_6 and NdB_6) [27,28], topological insulator state (SmB_6 and PuB_6) [29,30], and semiconductivity (CaB_6, SrB_6, and BaB_6) [31], making them of broad interest for industrial application.

Compared with the borides mentioned above, however, alkali metal borides are rarely investigated [32–37], which is mainly restricted by the difficult syntheses of these materials. Notably, theoretical simulations play a key role in accelerating the discovery of structures and broadening the understanding of traditional physics and chemistry knowledge. Many theoretical studies have been carried out on the structural stability and properties of alkali metal borides at ambient and high pressures. For instance, lithium borides, with a variety of stoichiometries, exhibit abundant boron motifs, i.e., from polyhedral boron framework to graphitelike sheets, zigzag chains, dimers, and eventually isolated B ions with increasing Li content [38,39]. A semiconducting $I2_12_12_1$-Na_2B_{30} structure was calculated to be more stable than the known *Imma*-Na_2B_{30} and possess a Vickers hardness value of 37.4 GPa at ambient pressure [40]. The negative linear compressibility and superionicity of NaB_3 have been revealed in recent theoretical work [41]. Cubic NaB_6 and KB_6 have been reported to possess superconductivity with predicted T_c of 15.7 and 14.6 K, respectively [42]. More interestingly, the removal of metal elements from binary compounds that are predicted to be stable under high pressure is considered an efficient route to obtain boron allotropes. For example, based on the precursors $I4/mmm$-NaB_4, Pm-Na_2B_{17}, and $C2/m$-KB_4, three metastable boron allotropes $I4/mmm$-B_4, Pm-B_{17}, and two-dimensional $C2/m$-structured boron have been proposed as

*liuguangtao@jlu.edu.cn

superconductors at ambient pressure with estimated T_c of 19.8, 15.4, and 17.9 K, respectively [43,44], which ignited a research boom in elemental superconductors.

In view of the above descriptions, alkali metal borides are expected to be a potential system with abundant structural types, providing a platform for searching for borides with appealing properties. Intuitively, rubidium (Rb) possesses a low electronegativity that should be conducive to transferring its electron to nonmetals (such as B) and forming corresponding compound(s). However, the relatively large atomic radius of Rb increases the distances between the B frameworks therein and weakens their interactions, resulting in no stable Rb-B compound at ambient pressure [45]. Accordingly, the Rb-B compounds are suggested to be stable at high pressure [45,46], which has been an effective tool for reducing atomic volumes and generating materials that are generally inaccessible under ambient conditions. Therefore, it remains of interest to further explore the crystal structures of compressed Rb-B compounds that may exhibit unanticipated physical properties and, equally, their important underlying mechanism.

In this paper, we have performed a theoretical investigation on the Rb-B binary system at a pressure range of 0–100 GPa. As a result, six stable stoichiometries of RbB, Rb_2B_3, RbB_3, RbB_6, RbB_8, and RbB_{10} were uncovered through the swarm intelligence structure prediction method. Among all these predicted structures, five stoichiometric Rb-B phases (e.g., $P6_3/mmc$-RbB, $C2/m$-RbB_3, Pm-3m-RbB_6, $Cmmm$-RbB_6, and $Immm$-RbB_8) are dynamically stable at atmospheric pressure and exhibit appealing structures and bonding behaviors with different boron concentrations. Furthermore, electron-phonon coupling (EPC) calculations indicate that metastable Pm-3m-RbB_6 and $Immm$-RbB_8 are superconductors with the estimated T_c of 7.3–11.6 and 4.8–7.5 K; more simulations suggest that some Rb-B compounds with three-dimensional structures are potentially superhard materials, with the highest Vickers hardness value of 36.9 GPa found in $Immm$-RbB_8. It is encouraging that $Immm$-RbB_8 could be a more suitable precursor to experimentally obtain the o-B_{16} boron allotrope at ambient pressure due to its superior stability. The present results expand the scope of research on the borides and showcase a feasible route to design unforeseen Rb-B compounds as potential functional materials.

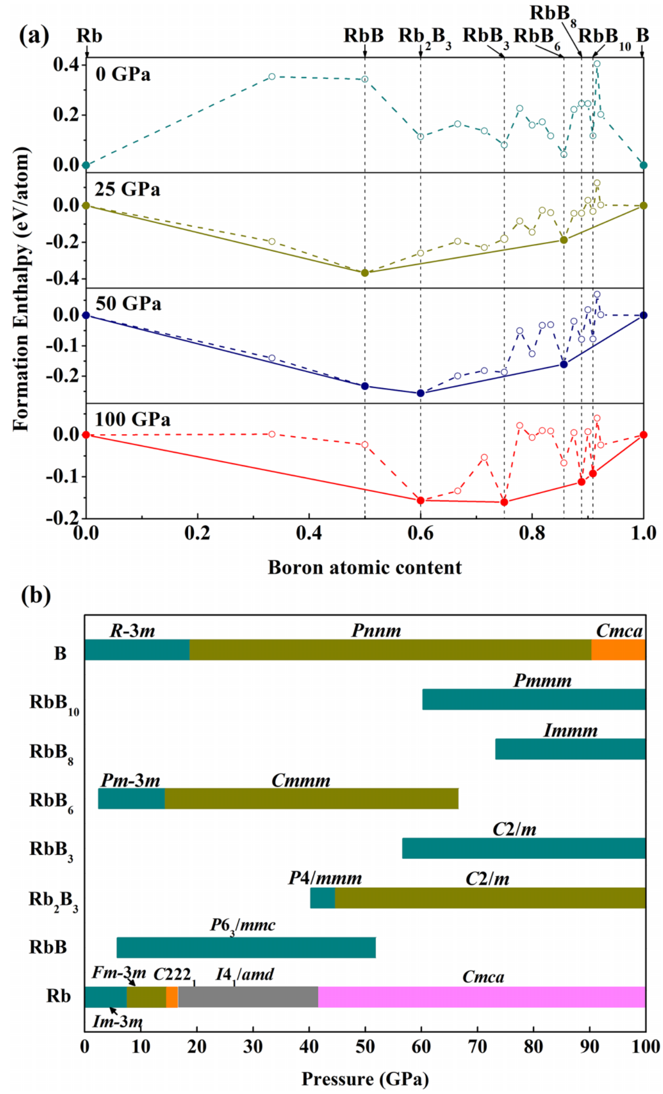

FIG. 1. (a) Thermodynamic stability of various Rb-B compounds with respect to elements Rb and B at selected pressures. The energetically stable stoichiometries are shown using solid symbols connected by solid lines on the convex hulls. (b) Pressure-composition phase stability diagram of the Rb-B system.

II. COMPUTATIONAL METHODS

Our structural prediction approach is based on a global minimization of free energy surfaces merging *ab initio* total-energy calculations through Crystal structure AnaLYsis by Particle Swarm Optimization (CALYPSO) methodology as implemented in its same-name CALYPSO code [47–49], which has been benchmarked on various known systems with several successful structure predictions [50,51]. The search for low-energy crystalline structures of Rb_xB_y ($x = 1$, $y = 1$–12; $x = 2$, $y = 1, 3, 5, 7$, and 9) was carried out using simulation cells with 1 and 2 f.u. at selected pressures of 0, 25, 50, and 100 GPa. In our simulations, each generation contained 40 structures, and the structures in the first generation were produced randomly. During structure evolution, 60% of structures in the first generation with lower enthalpies are selected to produce the structures in the next generation by the particle swarm optimization method, and 40% of the structures in the new generation are randomly generated. In most cases, structural searching simulations for each calculation are stopped after generating ∼1000 structures (e.g., ∼20–30 generations). The total number of predicted structures is at least ∼136 000 in the range of 0–100 GPa.

Our structural relaxations and electronic property calculations were performed within the Vienna *Ab initio* Simulation Package code within the framework of density functional theory [52]. The Perdew-Burke-Ernzerhof generalized gradient approximation [53] was chosen for the exchange-correlation functional. The ion-electron interaction is described by the projector augmented-wave (PAW) potential [54] with $4s^24p^65s^1$ and $2s^22p^1$ electrons as valence for Rb and B atoms, respectively. A plane-wave energy cutoff of 600 eV and Monkhorst-Pack k meshes with grid spacing of 0.20 Å^{-1}

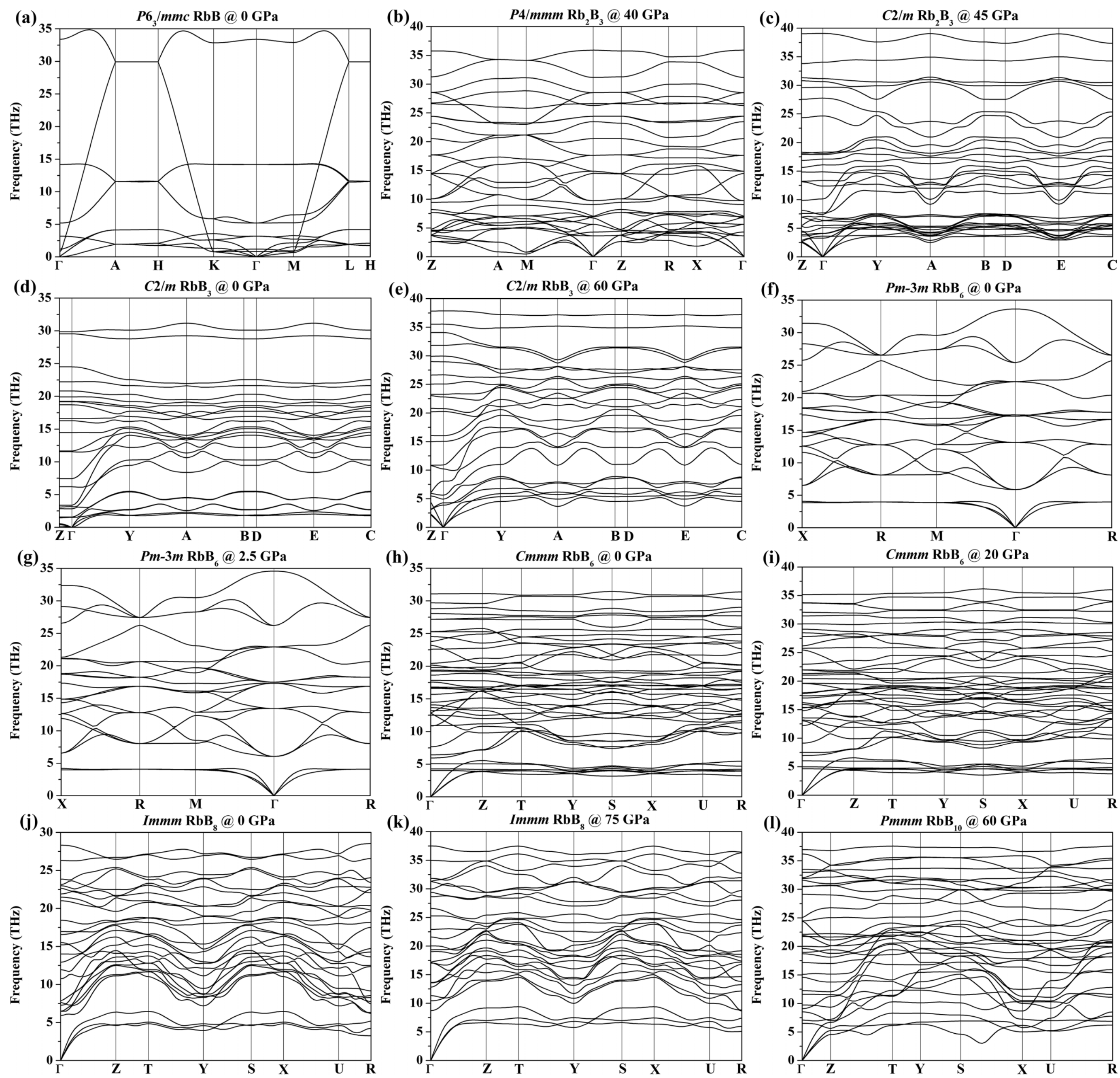

FIG. 2. Phonon dispersion curves of the predicted Rb-B phases.

for Brillouin zone sampling were employed to ensure total energy convergence to better than 1 meV/atom. The structures were fully relaxed until the energy and force were $< 10^{-6}$ eV and 0.01 eV/Å, respectively. Phonon calculations were carried out by using the linear response theory, which is implemented in the PHONOPY software [55].

The EPC calculations for superconducting properties were performed with density functional perturbation theory through the QUANTUM ESPRESSO code [56]. PAW pseudopotentials were used for Rb and B, with a kinetic energy cutoff of 80 Ry. The T_c was estimated by the standard Allen-Dynes modified McMillan equation [57]:

$$T_c = \frac{\omega_{\log}}{1.2} \exp\left[\frac{-1.04(1+\lambda)}{\lambda(1-0.62\mu^*)-\mu^*}\right],$$

where λ, $\omega_{\log}$, and μ^* represent the EPC strength, logarithmically averaged phonon frequency, and Coulomb repulsion coefficient, respectively. Vickers hardness was estimated by the microscopic hardness models [58,59].

III. RESULTS AND DISCUSSION

A. Structural stability

First, we investigated the thermodynamic stability of the binary Rb-B system by the calculation of their formation enthalpies relative to the dissociation products of Rb [60–63] and B [64] and constructed the convex hulls at pressures of 0, 25, 50, and 100 GPa, as shown in Fig. 1(a). In the view of energy, the thermodynamically stable structures are located on the solid lines of the convex hulls, while those on the dotted

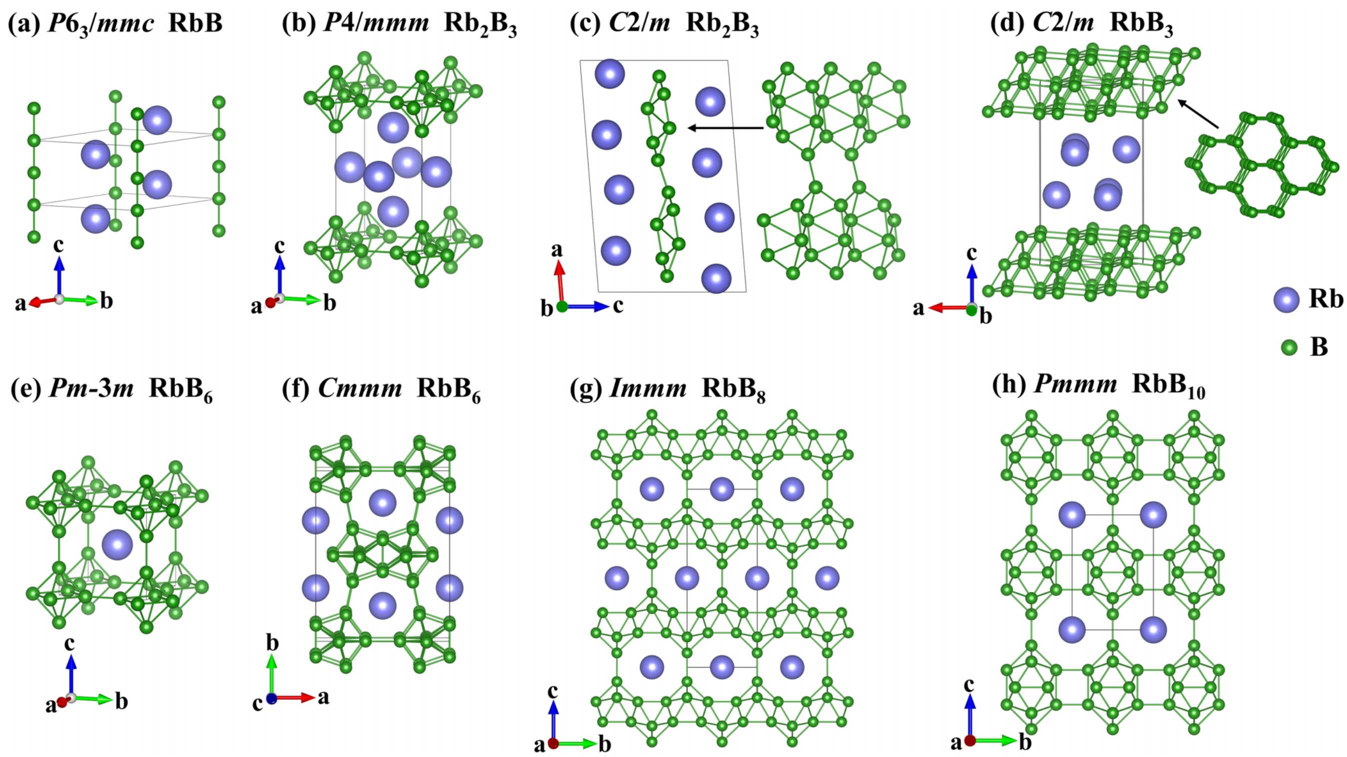

FIG. 3. Crystal structures of the Rb-B compounds under corresponding pressures. The Rb and B atoms are shown as big purple and small green spheres, respectively. (a) $P6_3/mmc$-RbB at 6 GPa, (b) $P4/mmm$-Rb_2B_3 at 40 GPa, (c) $C2/m$-Rb_2B_3 at 45 GPa, (d) $C2/m$-RbB_3 at 60 GPa, (e) Pm-3m-RbB_6 at 2.5 GPa, (f) $Cmmm$-RbB_6 at 15 GPa, (g) $Immm$-RbB_8 at 75 GPa, and (h) $Pmmm$-RbB_{10} at 60 GPa.

lines are thermodynamically unstable and tend to decompose into elements or other energetically stable binary compounds. Our result that no stoichiometry is stable at zero pressure is consistent with the previous research [45,46]. At 25 GPa, two stable compounds of RbB and RbB_6 lay on the convex hull, and RbB has the most negative enthalpy of formation. With increasing pressure to 50 GPa, Rb_2B_3 becomes thermodynamically stable as well. Upon further compression, three additional unexpected stoichiometries of RbB_3, RbB_8, and RbB_{10} appear, while RbB and RbB_6 are no longer stable. To accurately determine the pressure range of each stable Rb-B phase, we thus build the pressure-composition phase diagram, as shown in Fig. 1(b). The $P6_3/mmc$ structure of RbB is calculated to be stable between 5.8 and 52.0 GPa; $P4/mmm$-Rb_2B_3 is predicted to be stable in a small pressure range between 40.3 and 44.7 GPa and transform into an energetically favored $C2/m$ structure $>$ 44.7 GPa; and $C2/m$-RbB_3 is stabilized at 56.7 GPa and remains stable to at least 100 GPa. Additionally, the cubic Pm-3m phase of RbB_6 becomes stable $>$ 2.5 GPa, then converts to a $Cmcm$ phase at 14.4 GPa, and finally dissociates into RbB_3 and RbB_8 at 66.7 GPa. For the stoichiometries with a higher B content, $Immm$-RbB_8 and $Pmmm$-RbB_{10} are calculated to be stable $>$ 73.3 and 60.3 GPa, respectively. Moreover, we have examined the stability of stoichiometric Rb_3B_{20}, which was previously reported to be stable at moderate pressure relative to the elements Rb and B [45]. In our simulations, however, Rb_3B_{20} is unstable in the pressure range of 0–100 GPa once the abovementioned Rb-B compounds are considered.

We further performed phonon calculations to determine the dynamical stability of these proposed structures, as shown in Fig. 2. No imaginary phonon modes were found in the entire Brillouin zone of the studied structures, demonstrating these structures are dynamically stable under corresponding pressure. Notably, $P6_3/mmc$-RbB, $C2/m$-RbB_3, Pm-3m-RbB_6, $Cmmm$-RbB_6, and $Immm$-RbB_8 are dynamically stable at 0 GPa, indicating that they are likely to be quenched to ambient pressure for potential applications.

B. Crystal structures

To fundamentally understand these unprecedented Rb-B compounds under high pressures, the evolution of their crystal structure features with increasing B content is presented in Fig. 3. Hexagonal $P6_3/mmc$-RbB shows the same configuration as the known $P6_3/mmc$-LiB and KB [38,39,44], where B atoms exhibit one-dimensional chains along the c axis with a B-B bond length of 1.59 Å at 6 GPa [Fig. 3(a)]. Rb_2B_3 adopts a tetragonal ($P4/mmm$) structure at low pressure, in which B_6 octahedra occupy the vertex positions. High-pressure Rb_2B_3 and RbB_3 are monoclinic ($C2/m$) structures, and both can be viewed as two-dimensional sandwichlike structures with alternating buckled graphenelike boron slabs and Rb layers [Figs. 3(c) and 3(d)]. The low-pressure phase of RbB_6 adopts a CsCl-like structure with Pm-3m space group, in which the Rb atoms and B_6 octahedra replace the Cs and Cl sites. In this structure, the intraoctahedral and interoctahedral B-B distances are 1.80 and 1.70 Å at 2.5 GPa [Fig. 3(e)]. At elevated pressure, Pm-3m-RbB_6 is calculated to transform

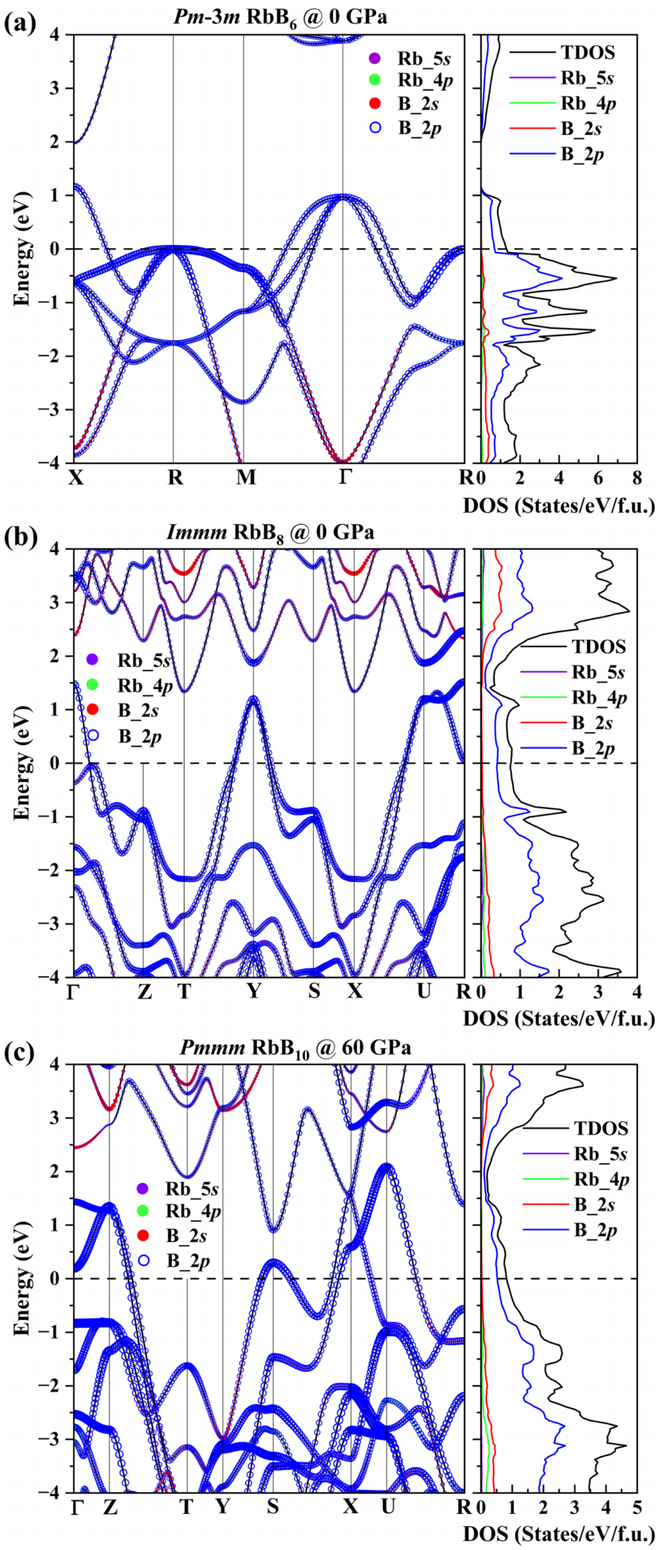

FIG. 4. Orbital-resolved band structures and density of states (DOS) for (a) Pm-$3m$-RbB_6 at 0 GPa, (b) $Immm$-RbB_8 at 0 GPa, and (c) $Pmmm$-RbB_{10} at 60 GPa. The horizontal dashed lines indicate Fermi energy levels. The size of the circles and dots represents the weights of the corresponding orbitals.

into an orthorhombic (*Cmmm*) structure. In this structure, two decahedral B_7 clusters are gathered by sharing an edge, forming a B_{12} cluster with B-B bond lengths of 1.66–1.89 Å at 15 GPa, where Rb atoms occupy interstitial positions in the lattice [Fig. 3(f)]. B-rich stoichiometric RbB_8 possesses an orthorhombic structure with *Immm* symmetry, which is isostructural to that of SrB_8 [65]. In this structure, B atoms form an open framework with B-B bond lengths of 1.65–1.85 Å at 75 GPa, while the Rb atom is located at the center of the boron framework [Fig. 3(g)]. B-richest stoichiometric RbB_{10} hosts an orthorhombic structure with *Pmmm* symmetry, consisting of a three-dimensional B framework with B-B bond lengths of 1.59–1.83 Å at 60 GPa, forming open channels parallel to the *a* axis to capture the Rb atoms [Fig. 3(h)]. In this Rb-B system, the arrangement of B atoms evolves from one-dimensional chains to two-dimensional layers, finally becoming a three-dimensional tunnel configuration with increased B element concentration. More structure information of predicted structures is summarized in Table S1 in the Supplemental Material [66].

C. Electronic properties

To further dig into the nature of their bonding characteristics, the electron localization functions (ELFs) [67,68] were calculated. Generally, high ELF values (>0.7) correspond to localized electrons in core or boning regions (covalent bonds) or lone pairs, whereas small values (<0.2) correspond to unshared electron interactions, such as ionic bonds or van der Waals bonds. The ELF values between 0.7 and 0.2 correspond to an electron localization like that of the electron-gas and indicate metallic bonds. As illustrated in Fig. S1 in the Supplemental Material [66], high ELF values are distributed between the neighboring B atoms, indicating that all B-B bonds are covalent. In contrast, no electron localization between Rb and B atoms demonstrates an ionic feature of the Rb-B bond, which is further evidenced by Bader charge analysis [69], where Rb apparently donates its electron (Table S2 in the Supplemental Material [66]). For all these stable Rb-B phases, each Rb atom transfers ~0.5 electrons to the B framework. Notably, for $C2/m$-RbB_3, Pm-$3m$-RbB_6, $Cmmm$-RbB_6, and $Immm$-RbB_8, some B atoms also transfer a low number of electrons (~0.1 *e*/atom) to other B atoms.

Since boron-rich metal borides usually have interesting electronic properties, we calculated the electronic band structures and projected density of states (PDOS) of these predicted Rb-B compounds, as shown in Fig. S2 in the Supplemental Material [66]. Except for semiconducting $Cmmm$-RbB_6, all the candidate structures exhibit metallic features with several bands crossing the Fermi level (Fig. S2 in the Supplemental Material [66]). $Cmmm$-RbB_6 exhibits semiconducting characteristics with a band gap of ~0.82 eV at 15 GPa (Fig. S2(f) in the Supplemental Material [66]). For $P6_3/mmc$-RbB, $P4/mmm$-Rb_2B_3, $C2/m$-Rb_2B_3, and $C2/m$-RbB_3, the densities of states (DOSs) at the Fermi level are dominated by the Rb atom, which is not beneficial to superconductivity; while for the more B-rich Pm-$3m$-RbB_6, $Immm$-RbB_8, and $Pmmm$-RbB_{10}, the contribution to the total DOS is mainly from B atoms, and the contribution from Rb atoms is negligible (Figs. S2(e), S2(g), and S2(h) in the Supplemental Material

TABLE I. Superconducting parameters of various Rb-B compounds.

Compounds	Space group	Pressure (GPa)	λ	ω_{log} (K)	N_{Ef} (states/spin/Ry/f.u.)	T_c (K) $\mu^* = 0.1$	T_c (K) $\mu^* = 0.13$
RbB_6	*Pm*-3*m*	0	0.52	797	12.1	11.6	7.3
RbB_6	*Pm*-3*m*	2.5	0.52	806	11.9	11.2	7.0
RbB_6	*Pm*-3*m*	14	0.51	826	11.4	10.8	6.7
RbB_8	*Immm*	0	0.54	464	5.2	7.5	4.8
RbB_8	*Immm*	30	0.41	604	4.7	2.9	1.3
RbB_8	*Immm*	75	0.31	783	4.4	0.5	0.1
RbB_{10}	*Pmmm*	60	0.40	514	5.6	2.0	0.9

[66]). This fact suggests that these more B-rich phases have the potential to exhibit high-T_c superconductivity, especially *Pm*-3*m*-RbB_6, which has a total DOS approximately twice as large as that of *Immm*-RbB_8 or *Pmmm*-RbB_{10}. Additionally, orbital-resolved band structures and DOSs for *Pm*-3*m*-RbB_6 at 0 GPa, *Immm*-RbB_8 at 0 GPa, and *Pmmm*-RbB_{10} at 60 GPa are also shown in Fig. 4. It can be clearly seen that the DOS near the Fermi level for these three structures is mainly from the contribution of B-2*p* orbitals.

D. Superconductivity

Motivated by the appearance of boron-dominated electronic DOS at the Fermi energy level for predicted *Pm*-3*m*-RbB_6, *Immm*-RbB_8, and *Pmmm*-RbB_{10}, we subsequently explored the superconductivity of these structures at different pressures through the Allen-Dynes modified McMillan equation using typical Coulomb pseudopotential parameters (μ^*) from 0.1 to 0.13 [57], as shown in Table I. As expected, the estimated T_c of *Pm*-3*m*-RbB_6 is ~11.6 (7.3) K with μ^* of 0.1 (0.13) at 0 GPa, which is the highest value in the Rb-B system. Although *Immm*-RbB_8 and *Pmmm*-RbB_{10} have higher B content than *Pm*-3*m*-RbB_6, the fewer electrons near the Fermi energy level cannot be effectively coupled with the lattice vibrations, resulting in both possessing relatively low superconductivity.

The phonon dispersions, projected phonon DOS (PHDOS), Eliashberg spectral function $\alpha^2F(\omega)/(\omega)$, and the integrated EPC strength $\lambda(\omega)$ for *Pm*-3*m*-RbB_6 and *Immm*-RbB_8 at 0 GPa are shown in Fig. 5. For *Pm*-3*m*-RbB_6 [Fig. 5(a)], the phonon dispersion curves and PHDOS show that frequencies <5 THz are dominated by Rb due to its large mass, while the high-frequency part is almost entirely driven by the vibrations of B atoms. It is noteworthy that the high-frequency part contributes ~97% to the total λ and mainly originates from the vibrations of B atoms. There are several strongly coupled phonon modes at 12–15 and 25–27 THz along the *X*-*R*-*M* path and around the Γ points, which contribute ~13 and ~4% to the total λ, respectively. More obviously, the acoustic modes from 15 to 20 THz along the entire Brillouin zone make great contributions to the EPC, which is also reflected in the Eliashberg spectral function $\alpha^2F(\omega)/(\omega)$, corresponding to a significant amount (~46%) of the total λ, and thus result in the relatively high superconducting T_c (11.6 K for $\mu^* = 0.1$) of *Pm*-3*m*-RbB_6. To probe the underlying causes, we further analyze several representative vibrational modes with relatively large EPC in this frequency range (e.g., E_g, B_{2g}, and T_{2g} modes at *X*, *M*, and Γ points, respectively; see Fig. S3 in the Supplemental Material [66]). These modes are all composed of bending vibrations of the diagonal atoms in the B_6 octahedron. Considering the dominant DOS of B-2*p*

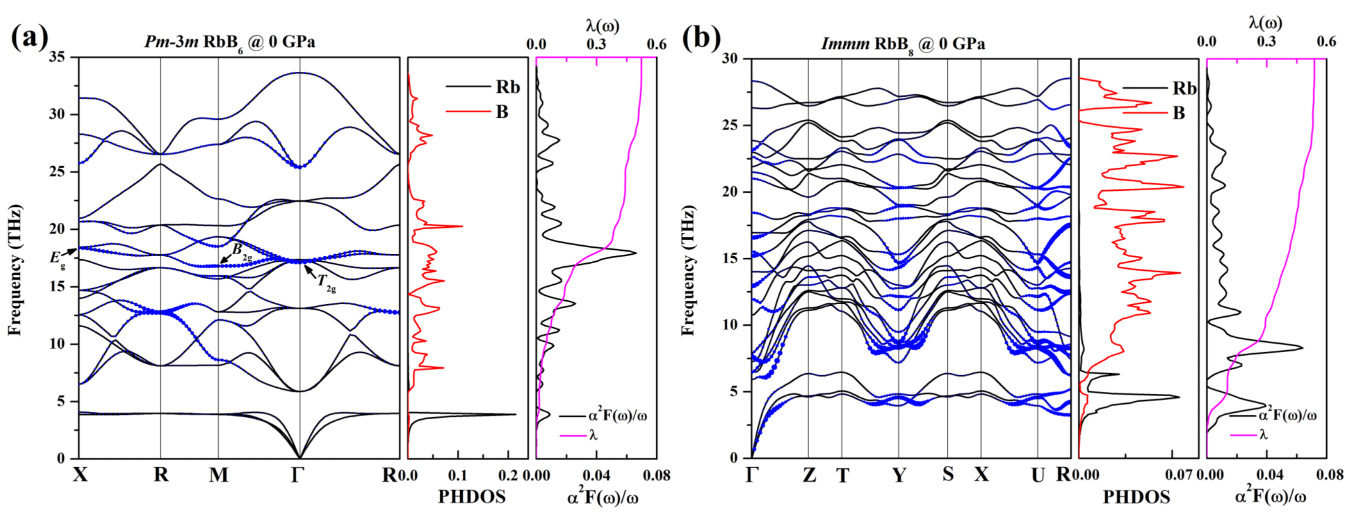

FIG. 5. Phonon dispersion relations, projected phonon density of states (PHDOS), Eliashberg function $\alpha^2F(\omega)/(\omega)$, and integrated electron-phonon coupling (EPC) strength $\lambda(\omega)$ of (a) *Pm*-3*m*-RbB_6 and (b) *Immm*-RbB_8 at 0 GPa. The size of the blue dots represents the magnitude of the EPC. Three representative strongly coupled phonon modes at 15–20 THz are marked with arrows in (a).

TABLE II. Hardness of various Rb-B compounds at ambient pressure.

Compounds	Space group	Hardness (GPa)	
		$H_{v,\text{ Chen}}$	$H_{v,\text{ Tian}}$
RbB_6	*Pm*-3*m*	19.7	18.6
RbB_6	*Cmmm*	31.1	28.7
RbB_8	*Immm*	36.9	34.4

orbitals at the Fermi level, we therefore conclude that the superconductivity of *Pm*-3*m*-RbB_6 mainly originates from the coupling between the electrons of B-2*p* orbitals and bending vibrations of the diagonal atoms in B_6 octahedron. For *Immm*-RbB_8 [Fig. 5(b)], coupling of electrons to phonons mainly originates from high-frequency vibrations in the range of 6–30 THz, which contribute 81% to the total λ. These frequencies are dominated by the vibrations of the B atoms, as in *Pm*-3*m*-RbB_6. The resulting T_c reaches a maximum value of 7.5 K using $\mu^* = 0.1$ at 0 GPa. Furthermore, the effects of pressure on the T_c were examined for *Pm*-3*m*-RbB_6 and *Immm*-RbB_8. The results show a decrease in T_c from 11.6 (7.5) K at 0 GPa to 10.8 (0.5) K at 14 (75) GPa for *Pm*-3*m*-RbB_6 (*Immm*-RbB_8) with a Coulomb potential μ^* of 0.1, which is attributed to the lattice hardening and the decrease of the total DOS at Fermi level with increasing pressure (see Table I).

E. Hardness

Because of the strong covalent B-B bonding, the Rb-B compounds are expected to possess high hardness. We first evaluated the mechanical properties of the predicted B-rich phases with the Voigt-Reuss-Hill approximation [70] at 0 GPa. Based on the empirical Vickers hardness methods [58,59], we calculated the hardness of these three B-rich phases, as listed in Table II. *Immm*-RbB_8 is a candidate for hard material with the highest hardness value in the Rb-B system. Its estimated Vickers hardness value is 36.9 GPa,

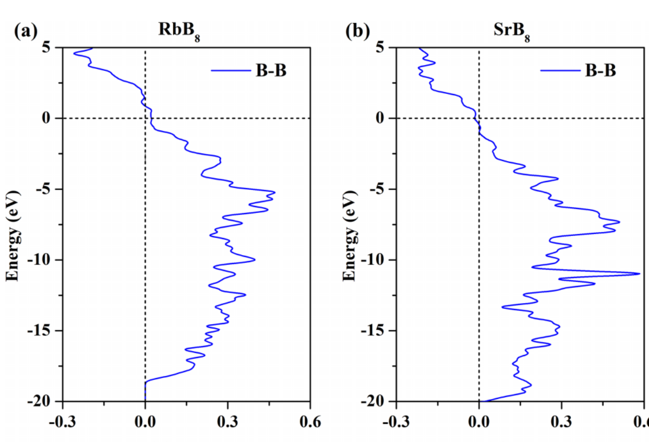

FIG. 6. Weighted average crystal orbital Hamiltonian population (COHP) of the seven B-B bonds in (a) RbB_8 and (b) SrB_8 at 75 GPa. The values of COHP > 0 and < 0 signify bonding states and antibonding states, respectively.

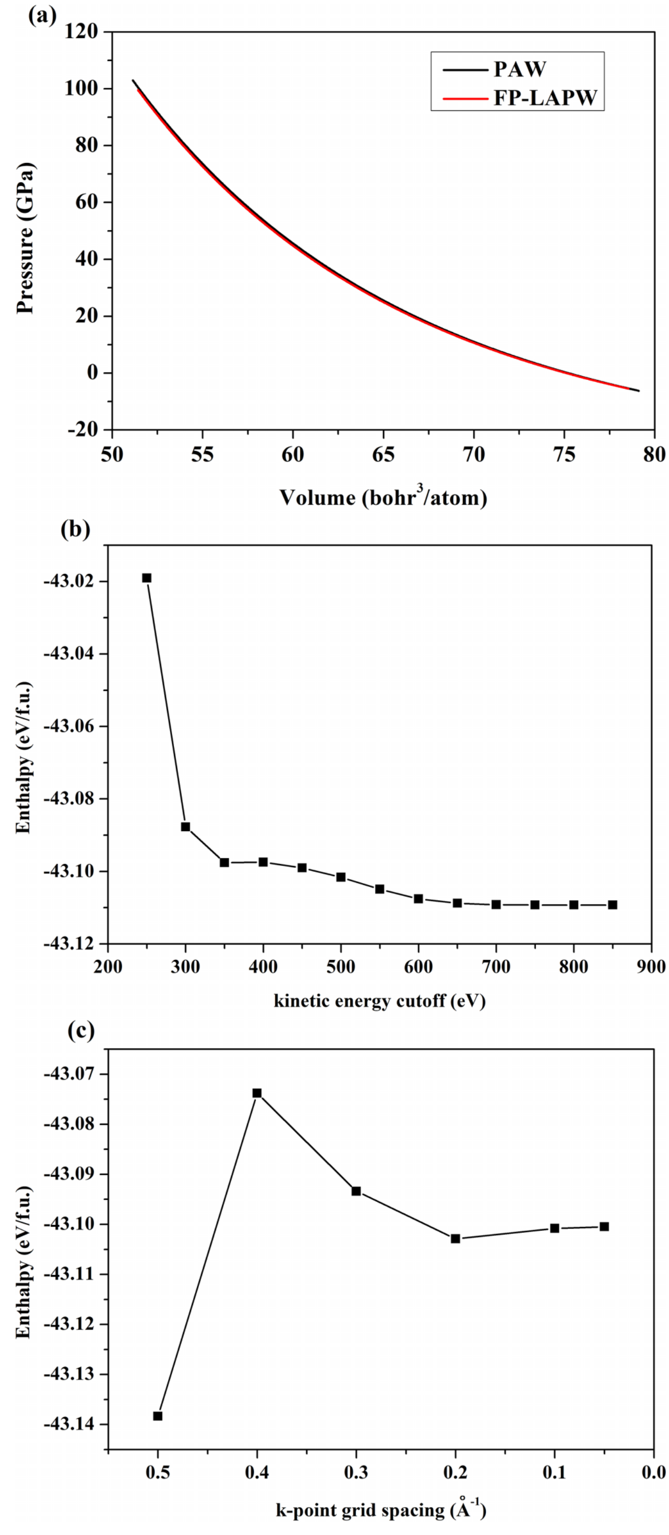

FIG. 7. (a) Comparison of the fitted Birch-Murnaghan equations of state for RbB_6 with *Pm*-3*m* symmetry by using the calculated results from the projector augmented-wave (PAW) pseudopotentials and the full-potential linearization augmented plane wave (FP-LAPW) methods. Convergence test of total energy relative to (b) plane-wave cutoff energy and (c) *k*-point grid spacing for *Pm*-3*m* RbB_6 at 0 GPa.

TABLE III. Calculated elastic constants C_{ij} (GPa), bulk modulus B (GPa), and shear modulus G (GPa), for Pm-3m-RbB_6, $Cmmm$-RbB_6, and $Immm$-RbB_8 at 0 GPa.

Phases	C_{11}	C_{22}	C_{33}	C_{44}	C_{55}	C_{66}	C_{12}	C_{13}	C_{23}	B	G
Pm-3m RbB_6	300.7	300.7	300.6	90.4	90.4	90.4	47.8	47.8	47.8	132.1	103.4
$Cmmm$ RbB_6	339.2	330.7	321.5	117.4	123.4	153.6	46.8	43.9	42.7	139.7	135.4
$Immm$ RbB_8	405.5	461.8	305.2	180.9	188.5	144.5	6.1	77.1	81.5	166.5	166.6

which is comparable with that of $I2_12_12_1$-Na_2B_{30} (37.4 GPa) [40] and $R3m$-YB_6 (37 GPa) [25] and slightly lower than that of ZrB_{12} (40 GPa) [24] and WB_4 (∼43 GPa) [22] at the load of 0.49 N.

F. Boron allotrope from RbB_8

Following the scheme of synthesis under high pressure and removal of metal atoms from precursors at ambient pressure, some allotropes have been successfully synthesized [71,72] or predicted [43,44,65,73]. Among them, an o-B_{16} boron allotrope may be available by removing the Sr atoms in channel-like SrB_8 [65]. However, since our calculation shows that SrB_8 is dynamically unstable at ambient pressure (Fig. S4 in the Supplemental Material [66]), it is still a challenge to obtain o-B_{16} boron allotrope from SrB_8 precursor. Here, we found that RbB_8, sharing the same boron structure as SrB_8, is not only dynamically stable at ambient pressure but also possesses superior thermodynamic stability. To further understand its stability mechanism, we used the crystal orbital Hamilton population (COHP) [74] to analyze the bonding character of the states around the Fermi level of RbB_8 and SrB_8. The COHP analysis aims to measure weighted population of wave functions on two atomic orbitals of a pair of selected atoms, which is implemented in the LOBSTER-4.0.0 program [75]. The values of COHP > 0 and < 0 signify bonding states and antibonding states, respectively. The COHPs in Fig. 6 show that the antibonding character of occupied states around the Fermi level is unambiguous between B-B atoms in SrB_8, owing to Sr donating more electrons to occupy the antibond orbit. For Rb that has only one valence electron, no occupied antibonding states are exhibited in RbB_8, which results in a decrease in energy of the system and is a more suitable precursor for the synthesis of the o-B_{16} boron allotrope.

IV. CONCLUSIONS

We have systematically studied the crystal structures and physical properties of the Rb-B compounds at the pressure range of 0–100 GPa using the swarm intelligence structure search method combined with first-principles calculations. Six thermodynamically stable phases of RbB, Rb_2B_3, RbB_3, RbB_6, RbB_8, and RbB_{10} have been established. Among these predicted structures, Pm-3m-RbB_6 and $Immm$-RbB_8 exhibit superconductivity with estimated T_c of 11.6 and 7.5 K at ambient pressure. Further analysis of electronic and phonon properties indicates that the superconducting mainly originates from the coupling between the B-2p orbitals and the high-frequency vibrations of the B atoms. In addition, the predicted Vickers hardness (36.9 GPa) indicates that $Immm$-RbB_8 is a potential hard material. Encouragingly, given the robust stability of $Immm$-RbB_8, it is a more suitable precursor to obtain the o-B_{16} boron allotrope experimentally. The current findings not only deepen the understanding of the high-pressure behavior of the alkali metal borides family but also stimulate future experimental and theoretical investigations on the Rb-B compounds.

ACKNOWLEDGMENTS

This paper was supported by the National Key Research and Development Program of China (Grant No. 2021YFA1400203), the Major Program of the National Natural Science Foundation of China (Grant No. 52090024), National Natural Science Foundation of China (Grants No. 12074138 and No. 12074139), Jilin Province Science and Technology Development Program (Grant No. YDZJ202102CXJD016), Program for Jilin University Science and Technology Innovative Research Team, the Program for Jilin University Computational Interdisciplinary Innovative Platform, the Strategic Priority Research Program of Chinese Academy of Sciences (Grant No. XDB33000000), and computing facilities at the High-Performance Computing Centre of Jilin University and computing facilities at HOKUSAI system in RIKEN (Japan).

APPENDIX

The full-potential linearization augmented plane wave (FP-LAPW) method as implemented in the WIEN2K code [76] was used to check the equation of state for Pm-3m-RbB_6. The result of FP-LAPW is highly consistent with that of pseudopotential calculation, as shown in Fig. 7(a), confirming the reliability of the adopted pseudopotentials in this paper. To ensure good convergence of total energy, we have performed the convergence test of total energy relative to plane-wave cutoff energy and k-point grid spacing for Pm-3m RbB_6 at 0 GPa, as shown in Figs. 7(b) and 7(c). The plane-wave cutoff energy of 600 eV and Monkhorst-Pack k meshes with grid spacing of 0.20 $Å^{-1}$ are sufficient to ensure good convergence of total energy.

We have evaluated the mechanical properties of the predicted B-rich phases with the Voigt-Reuss-Hill approximation [70] at 0 GPa. The results in Table III show that Pm-3m-RbB_6, $Cmmm$-RbB_6, and $Immm$-RbB_8 are all mechanically stable.

The cubic Pm-3m-RbB_6 structure satisfies the following mechanical stability criteria:

$$C_{11} > 0,\ C_{44} > 0,\ C_{11} > |C_{12}|,\ (C_{11} + 2C_{12}) > 0.$$

The orthorhombic $Cmmm$-RbB_6 and $Immm$-RbB_8 structures satisfy the following mechanical stability criteria:

$$C_{11} > 0,\ C_{22} > 0,\ C_{33} > 0,\ C_{44} > 0,\ C_{55} > 0,\ C_{66} > 0,$$

$$[C_{11} + C_{22} + C_{33} + 2(C_{12} + C_{13} + C_{23})] > 0,$$
$$(C_{11} + C_{22} - 2C_{12}) > 0,$$
$$(C_{11} + C_{33} - 2C_{13}) > 0,$$
$$(C_{22} + C_{33} - 2C_{23}) > 0.$$

[1] B. Albert and H. Hillebrecht, Boron: Elementary challenge for experimenters and theoreticians, Angew. Chemie Int. Ed. **48**, 8640 (2009).

[2] G. Akopov, M. T. Yeung, and R. B. Kaner, Rediscovering the crystal chemistry of borides, Adv. Mater. **29**, 1604506 (2017).

[3] J. Nagamatsu, N. Nakagawa, T. Muranaka, Y. Zenitani, and J. Akimitsu, Superconductivity at 39 K in magnesium diboride, Nature (London) **410**, 63 (2001).

[4] C. Buzea and T. Yamashita, Review of the superconducting properties of MgB_2, Supercond. Sci. Technol. **14**, R115 (2001).

[5] R. Lortz, Y. Wang, U. Tutsch, S. Abe, C. Meingast, P. Popovich, W. Knafo, N. Shitsevalova, Y. B. Paderno, and A. Junod, Superconductivity mediated by a soft phonon mode: Specific heat, resistivity, thermal expansion, and magnetization of YB_6, Phys. Rev. B **73**, 024512 (2006).

[6] Y. Singh, A. Niazi, M. Vannette, R. Prozorov, and D. Johnston, Superconducting and normal-state properties of the layered boride OsB_2, Phys. Rev. B **76**, 214510 (2007).

[7] H. Gou, N. Dubrovinskaia, E. Bykova, A. A. Tsirlin, D. Kasinathan, W. Schnelle, A. Richter, M. Merlini, M. Hanfland, A. M. Abakumov *et al.*, Discovery of a Superhard Iron Tetraboride Superconductor, Phys. Rev. Lett. **111**, 157002 (2013).

[8] G. Akopov, W. H. Mak, D. Koumoulis, H. Yin, B. Owens-Baird, M. T. Yeung, M. H. Muni, S. Lee, I. Roh, Z. C. Sobell *et al.*, Synthesis and characterization of single-phase metal dodecaboride solid solutions: $Zr_{1-x}Y_xB_{12}$ and $Zr_{1-x}U_xB_{12}$, J. Am. Chem. Soc. **141**, 9047 (2019).

[9] J. Teyssier, A. Kuzmenko, D. van der Marel, F. Marsiglio, A. Liashchenko, N. Shitsevalova, and V. Filippov, Optical study of electronic structure and electron-phonon coupling in ZrB_{12}, Phys. Rev. B **75**, 134503 (2007).

[10] C. Pei, J. Zhang, Q. Wang, Y. Zhao, L. Gao, C. Gong, S. Tian, R. Luo, Z.-Y. Lu, H. Lei, K. Liu, and Y. Qi, Pressure-induced superconductivity at 32 K in MoB_2, arXiv:2105.13250v1 (2021).

[11] H. J. Choi, S. G. Louie, and M. L. Cohen, Prediction of superconducting properties of CaB_2 using anisotropic Eliashberg theory, Phys. Rev. B **80**, 064503 (2009).

[12] L. Ma, X. Yang, G. Liu, H. Liu, G. Yang, H. Wang, J. Cai, M. Zhou, and H. Wang, Design and synthesis of clathrate LaB_8 with superconductivity, Phys. Rev. B **104**, 174112 (2021).

[13] Y. Liang, M. Xu, S. Lin, X. Yuan, Z. Qu, J. Hao, and Y. Li, Pressure-induced boron clathrates with ambient-pressure superconductivity, J. Mater. Chem. C **9**, 13782 (2021).

[14] L. Wu, B. Wan, H. Liu, H. Gou, Y. Yao, Z. Li, J. Zhang, F. Gao, and H.-k. Mao, Coexistence of superconductivity and superhardness in beryllium hexaboride driven by inherent multicenter bonding, J. Phys. Chem. Lett. **7**, 4898 (2016).

[15] L. Duan, J. Su, N. Gong, B. Wan, P. Chen, P. Zhou, Z. Wang, Z. Li, and L. Wu, Pressure induced semiconductor-semimetal-superconductor transition of magnesium hexaborides, Dalton Trans. **48**, 14299 (2019).

[16] J. K. Dewhurst, S. Sharma, C. Ambrosch-Draxl, and B. Johansson, First-principles calculation of superconductivity in hole-doped LiBC: $T_c = 65\,\mathrm{K}$, Phys. Rev. B **68**, 020504(R) (2003).

[17] G. Akopov, L. E. Pangilinan, R. Mohammadi, and R. B. Kaner, Perspective: Superhard metal borides: A look forward, APL Mater. **6**, 070901 (2018).

[18] M. T. Yeung, R. Mohammadi, and R. B. Kaner, Ultraincompressible, superhard materials, Annu. Rev. Mater. Res. **46**, 465 (2016).

[19] L. E. Pangilinan, S. Hu, G. Akopov, S. C. Cabrera, M. T. Yeung, R. Mohammadi, S. H. Tolbert, and R. B. Kaner, Superhard materials: Advances in the search and synthesis of new materials, in *Encyclopedia of Inorganic and Bioinorganic Chemistry*, edited by R. A. Scott (John Wiley & Sons, Ltd., Hoboken, 2023).

[20] H.-Y. Chung, M. B. Weinberger, J. B. Levine, A. Kavner, J.-M. Yang, S. H. Tolbert, and R. B. Kaner, Synthesis of ultra-incompressible superhard rhenium diboride at ambient pressure, Science **316**, 436 (2007).

[21] R. W. Cumberland, M. B. Weinberger, J. J. Gilman, S. M. Clark, S. H. Tolbert, and R. B. Kaner, Osmium diboride, an ultra-incompressible, hard material, J. Am. Chem. Soc. **127**, 7264 (2005).

[22] R. Mohammadi, A. T. Lech, M. Xie, B. E. Weaver, M. T. Yeung, S. H. Tolbert, and R. B. Kaner, Tungsten tetraboride, an inexpensive superhard material, Proc. Natl. Acad. Sci. USA **108**, 10958 (2011).

[23] H. Niu, J. Wang, X.-Q. Chen, D. Li, Y. Li, P. Lazar, R. Podloucky, and A. N. Kolmogorov, Structure, bonding, and possible superhardness of CrB_4, Phys. Rev. B **85**, 144116 (2012).

[24] T. Ma, H. Li, X. Zheng, S. Wang, X. Wang, H. Zhao, S. Han, J. Liu, R. Zhang, P. Zhu *et al.*, Ultrastrong boron frameworks in ZrB_{12}: A highway for electron conducting, Adv. Mater. **29**, 1604003 (2017).

[25] L.-P. Ding, Y. H. Tiandong, P. Shao, Y. Tang, Z.-L. Zhao, and H. Lu, Crystal structures, phase stabilities, electronic properties, and hardness of yttrium borides: New insight from first-principles calculations, J. Phys. Chem. Lett. **12**, 5423 (2021).

[26] K. Zhao, Q. Wang, W. Li, Q. Yang, H. Yu, F. Han, H. Liu, and S. Zhang, Orthorhombic ScB_3 and hexagonal ScB_6 with high hardness, Phys. Rev. B **105**, 094104 (2022).

[27] X. Ji, Q. Zhang, J. Xu, and Y. Zhao, Rare-earth hexaborides nanostructures: Recent advances in materials, characterization and investigations of physical properties, Prog. Solid State Ch. **39**, 51 (2011).

[28] J. Xu, G. Hou, T. Mori, H. Li, Y. Wang, Y. Chang, Y. Luo, B. Yu, Y. Ma, and T. Zhai, Excellent field-emission performances of neodymium hexaboride (NdB_6) nanoneedles with ultra-low work functions, Adv. Funct. Mater. **23**, 5038 (2013).

[29] D.-J. Kim, J. Xia, and Z. Fisk, Topological surface state in the Kondo insulator samarium hexaboride, Nat. Mater. **13**, 466 (2014).
[30] X. Deng, K. Haule, and G. Kotliar, Plutonium Hexaboride is a Correlated Topological Insulator, Phys. Rev. Lett. **111**, 176404 (2013).
[31] B. Huang, Y.-H. Duan, Y. Sun, M.-J. Peng, and S. Chen, Electronic structures, mechanical and thermodynamic properties of cubic alkaline-earth hexaborides from first principles calculations, J. Alloy. Compd. **635**, 213 (2015).
[32] M. Wörle, R. Nesper, and T. K. Chatterji, LiB_x ($0.82 < x \leqslant 1.0$)-an incommensurate composite structure below 150 K, Z. anorg. allg. Chem. **632**, 1737 (2006).
[33] G. Mair, R. Nesper, and H. G. von Schnering, Trilithium tetradecaboride Li_3B_{14}: Synthesis, structure, and properties, J. Solid State Chem. **75**, 30 (1988).
[34] G. Mair, H. G. von Schnering, M. Wörle, and R. Nesper, Dilithium hexaboride, Li_2B_6, Z. anorg. allg. Chem. **625**, 1207 (1999).
[35] B. Albert, K. Hofmann, C. Fild, H. Eckert, M. Schleifer, and R. Gruehn, "NaB_{15}": A new structural description based on x-ray and neutron diffraction, electron microscopy, and solid-state NMR spectroscopy, Chem. Eur. J. **6**, 2531 (2000).
[36] B. Albert, A new "old" sodium boride: Linked pentagonal bipyramids and octahedra in Na_3B_{20}, Angew. Chem. Int. Edit. **37**, 1117 (1998).
[37] A. Ammar, M. Ménétrier, A. Villesuzanne, S. Matar, B. Chevalier, J. Etourneau, G. Villeneuve, J. Rodríguez-Carvajal, H.-J. Koo, and A. Smirnov, Investigation of the electronic and structural properties of potassium hexaboride, KB_6, by transport, magnetic susceptibility, EPR, and NMR measurements, temperature-dependent crystal structure determination, and electronic band structure calculations, Inorg. Chem. **43**, 4974 (2004).
[38] F. Peng, M. Miao, H. Wang, Q. Li, and Y. Ma, Predicted lithium-boron compounds under high pressure, J. Am. Chem. Soc. **134**, 18599 (2012).
[39] A. Hermann, A. McSorley, N. W. Ashcroft, and R. Hoffmann, From Wade-Mingos to Zintl-Klemm at 100 GPa: Binary compounds of boron and lithium, J. Am. Chem. Soc. **134**, 18606 (2012).
[40] X.-L. He, X. Dong, Q. Wu, Z. Zhao, Q. Zhu, A. R. Oganov, Y. Tian, D. Yu, X.-F. Zhou, and H.-T. Wang, Predicting the ground-state structure of sodium boride, Phys. Rev. B **97**, 100102(R) (2018).
[41] X.-L. He, S.-N. Pan, Y. Chen, X.-J. Weng, Z. Wang, D. Yu, X. Dong, J. Sun, Y. Tian, and X.-F. Zhou, Negative linear compressibility and unusual dynamic behavior of NaB_3, Phys. Rev. Mater. **5**, 035002 (2021).
[42] Z. Yuan, L. Hao, K. Luo, M. Xiong, C. Shao, F. Ling, and D. Yu, Structural stability, electronic structure, and superconductivity of cubic sodium hexaboride NaB_6 from first-principle calculations, Chem. Phys. Lett. **722**, 80 (2019).
[43] S. Zhang, X. Du, J. Lin, A. Bergara, X. Chen, X. Liu, X. Zhang, and G. Yang, Superconducting boron allotropes, Phys. Rev. B **101**, 174507 (2020).
[44] T. Chen, Q. Gu, Q. Chen, X. Wang, C. J. Pickard, R. J. Needs, D. Xing, and J. Sun, Prediction of quasi-one-dimensional superconductivity in metastable two-dimensional boron, Phys. Rev. B **101**, 054518 (2020).
[45] A. N. Kolmogorov and S. Curtarolo, Theoretical study of metal borides stability, Phys. Rev. B **74**, 224507 (2006).
[46] A. Van Der Geest and A. Kolmogorov, Stability of 41 metal-boron systems at 0 GPa and 30 GPa from first principles, Calphad **46**, 184 (2014).
[47] Y. Wang, J. Lv, L. Zhu, and Y. Ma, Crystal structure prediction via particle-swarm optimization, Phys. Rev. B **82**, 094116 (2010).
[48] Y. Wang, J. Lv, L. Zhu, and Y. Ma, CALYPSO: A method for crystal structure prediction, Comput. Phys. Commun. **183**, 2063 (2012).
[49] X. Shao, J. Lv, P. Liu, S. Shao, P. Gao, H. Liu, Y. Wang, and Y. Ma, A symmetry-orientated divide-and-conquer method for crystal structure prediction, J. Chem. Phys. **156**, 014105 (2022).
[50] J. Zhang, H. Liu, Y. Ma, and C. Chen, Direct H-He chemical association in superionic FeO_2H_2He at deep-earth conditions, Natl. Sci. Rev. **9**, nwab168 (2022).
[51] X. Zhong, Y. Sun, T. Iitaka, M. Xu, H. Liu, R. J. Hemley, C. Chen, and Y. Ma, Prediction of above-room-temperature superconductivity in lanthanide/actinide extreme superhydrides, J. Am. Chem. Soc. **144**, 13394 (2022).
[52] G. Kresse and J. Furthmüller, Efficient iterative schemes for *ab initio* total-energy calculations using a plane-wave basis set, Phys. Rev. B **54**, 11169 (1996).
[53] J. P. Perdew, K. Burke, and M. Ernzerhof, Generalized Gradient Approximation Made Simple, Phys. Rev. Lett. **77**, 3865 (1996).
[54] P. E. Blöchl, Projector augmented-wave method, Phys. Rev. B **50**, 17953 (1994).
[55] A. Togo and I. Tanaka, First principles phonon calculations in materials science, Scripta Mater. **108**, 1 (2015).
[56] P. Giannozzi, S. Baroni, N. Bonini, M. Calandra, R. Car, C. Cavazzoni, D. Ceresoli, G. L. Chiarotti, M. Cococcioni, I. Dabo *et al.*, QUANTUM ESPRESSO: A modular and open-source software project for quantum simulations of materials, J. Phys.: Condens. Matter **21**, 395502 (2009).
[57] P. B. Allen and R. Dynes, Transition temperature of strong-coupled superconductors reanalyzed, Phys. Rev. B **12**, 905 (1975).
[58] X.-Q. Chen, H. Niu, D. Li, and Y. Li, Modeling hardness of polycrystalline materials and bulk metallic glasses, Intermetallics **19**, 1275 (2011).
[59] Y. Tian, B. Xu, and Z. Zhao, Microscopic theory of hardness and design of novel superhard crystals, Int. J. Refract. Met. H. **33**, 93 (2012).
[60] K. Takemura and K. Syassen, High pressure equation of state of rubidium, Solid State Commun. **44**, 1161 (1982).
[61] R. Nelmes, M. McMahon, J. Loveday, and S. Rekhi, Structure of Rb-III: Novel Modulated Stacking Structures in Alkali Metals, Phys. Rev. Lett. **88**, 155503 (2002).
[62] U. Schwarz, K. Syassen, A. Grzechnik, and M. Hanfland, The crystal structure of rubidium-VI near 50 GPa, Solid State Commun. **112**, 319 (1999).
[63] Y. Ma, A. R. Oganov, and Y. Xie, High-pressure structures of lithium, potassium, and rubidium predicted by an *ab initio* evolutionary algorithm, Phys. Rev. B **78**, 014102 (2008).
[64] A. R. Oganov, J. Chen, C. Gatti, Y. Ma, Y. Ma, C. W. Glass, Z. Liu, T. Yu, O. O. Kurakevych, and V. L. Solozhenko, Ionic

high-pressure form of elemental boron, Nature (London) **457**, 863 (2009).

[65] Z. Cui, Q. Yang, X. Qu, X. Zhang, Y. Liu, and G. Yang, A superconducting boron allotrope featuring anticlinal pentapyramids, J. Mater. Chem. C **10**, 672 (2022).

[66] See Supplemental Material at http://link.aps.org/supplemental/10.1103/PhysRevResearch.5.013130 for ELFs, electronic band structures, and PDOS of predicted Rb-B phases; visualization of several representative vibration modes of *Pm-3m*-RbB6 at 1 atm; phonon dispersion curves of *Immm*-SrB8 at 1 atm; and detail structural information and Bader charge analysis of predicted Rb-B compounds at selected pressures.

[67] A. D. Becke and K. E. Edgecombe, A simple measure of electron localization in atomic and molecular systems, J. Chem. Phys. **92**, 5397 (1990).

[68] K. Koumpouras and J. A. Larsson, Distinguishing between chemical bonding and physical binding using electron localization function (ELF), J. Phys: Condens. Matter. **32**, 315502 (2020).

[69] R. F. Bader, Atoms in molecules, Acc. Chem. Res. **18**, 9 (1985).

[70] R. Hill, The elastic behaviour of a crystalline aggregate, Proc. Phys. Soc. A **65**, 349 (1952).

[71] D. Y. Kim, S. Stefanoski, O. O. Kurakevych, and T. A. Strobel, Synthesis of an open-framework allotrope of silicon, Nat. Mater. **14**, 169 (2015).

[72] H.-J. Sung, W. H. Han, I.-H. Lee, and K. J. Chang, Superconducting Open-Framework Allotrope of Silicon at Ambient Pressure, Phys. Rev. Lett. **120**, 157001 (2018).

[73] Y. Liang, M. Xu, Z. Qu, S. Lin, J. Hao, and Y. Li, A cage boron allotrope with high superconductivity at ambient pressure, J. Mater. Chem. C **9**, 8258 (2021).

[74] R. Dronskowski and P. E. Bloechl, Crystal orbital Hamilton populations (COHP): Energy-resolved visualization of chemical bonding in solids based on density-functional calculations, J. Phys. Chem. **97**, 8617 (1993).

[75] R. Nelson, C. Ertural, J. George, V. L. Deringer, G. Hautier, and R. Dronskowski, LOBSTER: Local orbital projections, atomic charges, and chemical-bonding analysis from projector-augmented-wave-based density-functional theory, J. Comput. Chem. **41**, 1931 (2020).

[76] P. Blaha, K. Schwarz, P. Sorantin, and S. Trickey, Full-potential, linearized augmented plane wave programs for crystalline systems, Comput. Phys. Commun. **59**, 399 (1990).